Editing Scene Illumination and Material Appearance of Light-Field Images

Jaemin Cho[1][a], Dongyoung Choi[1][b], Dahyun Kang[1][c], Gun Bang[2][d] and Min H. Kim[1][e]

[1]*School of Computing, KAIST, Daejeon, South Korea*

[2]*Research Department of Media Coding, ETRI, Deajeon, South Korea*

{jmcho,dychoi}@vclab.kaist.ac.kr, 313usually@gmail.com, gbang@etri.re.kr, minhkim@kaist.ac.kr

Keywords: Light-field image decomposition, scene illumination, neural inverse rendering

Abstract: In this paper, we propose a method for editing the scene appearance of light-field images. Our method enables users to manipulate the illumination and material properties of scenes captured in light-field format, offering various control over image appearance, including dynamic relighting and material appearance modification, which leverages our specially designed inverse rendering framework for light-field images. By effectively separating light fields into appearance parameters—such as diffuse albedo, normal, specular intensity, and roughness within a multi-plane image domain, we overcome the traditional challenges of light-field imaging decomposition. These challenges include handling front-parallel views and a limited image count, which have previously hindered neural inverse rendering networks when applying them to light-field image data. Our method also approximates environmental illumination using spherical Gaussians, significantly enhancing the realism of scene reflectance. Furthermore, by differentiating scene illumination into far-bound and near-bound light environments, our method enables highly realistic editing of scene appearance and illumination, especially for local illumination effects. This differentiation allows for efficient, real-time relighting rendering and integrates seamlessly with existing layered light-field rendering frameworks. Our method demonstrates rendering capabilities from casually captured light-field images.

1 INTRODUCTION

Light-field cameras and devices have revolutionized image capture and processing in computer vision and graphics, enabling various applications in novel view synthesis (Gortler et al., 1996; Choi et al., 2019; Riegler and Koltun, 2020; Riegler and Koltun, 2021), scene editing (Jarabo et al., 2014; Mihara et al., 2016), and augmented reality (Holynski and Kopf, 2018). By capturing multiple sub-aperture images, they provide a depth of scene information far beyond what traditional cameras can offer.

In this paper, we propose a method that allows for scene editing through our novel decomposition of light-field images. We target key appearance parameters—diffuse albedo, normals, specular intensity, and roughness—within the multi-plane image (MPI) domain (Zhou et al., 2018). This technique not only captures but enhances the realism of environmental illumination, thereby effectively editing material appear-

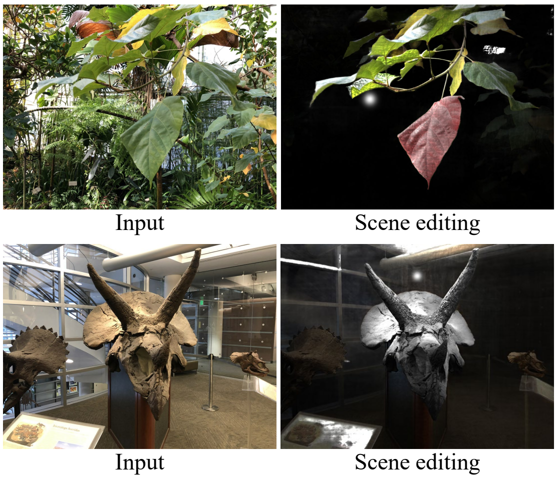

Figure 1: We present a method to decompose light-field images into illumination and intrinsic appearance parameters, enabling realistic relighting and material editing. Refer to our supplemental video for additional results.

[a] https://orcid.org/0000-0003-2800-5105
[b] https://orcid.org/0000-0003-1896-4038
[c] https://orcid.org/0000-0003-2632-0048
[d] https://orcid.org/0000-0003-4355-599X
[e] https://orcid.org/0000-0002-5078-4005

ance and scene relighting in casually captured light-field images as shown in Figure 1.

Despite the richness of the light-field image data, processing light-field images still presents unique challenges. Their sub-aperture images typically exhibit front-parallel view directions and a limited count range, complicating the creation of comprehensive 3D models and the extraction of material appearance parameters. Furthermore, the conventional methods for light-field imaging often fall short in depicting specular reflections accurately due to their reliance on viewing direction, a limitation that each pixel maintains a constant value, regardless of the angle of view (Flynn et al., 2019; Mildenhall et al., 2019; Zhou et al., 2018).

Addressing these challenges, we introduce a neural inverse rendering method especially tailored for *scene-scale* light-field inputs within the MPI domain. Our method employs spherical Gaussian approximations to segment the light environment into far-bound and near-bound regions, capturing both global and local illumination variations essential for realistic scene appearance manipulation. The overall process of our method is visualized in Figure 2. From a given light-field image, our method decomposes sub-aperture images into appearance parameters (diffuse albedo, normal, specular intensity, and roughness) in multi-plane image space, along with global/local scene illumination represented as spherical Gaussian functions. The MPI has 9 channels, with the number next to each appearance parameter indicating the number of channels representing that parameter. These decomposed elements enable the manipulation of scene appearance and illumination at a scene-wide scale, not just for individual objects. This approach not only boosts rendering efficiency but also ensures seamless integration with existing light-field rendering architectures (Flynn et al., 2019; Mildenhall et al., 2019).

By demonstrating practical applications ranging from relighting to material appearance changes, our work showcases the versatility and effectiveness of our method in enhancing the realism and applicability of light-field imaging for scene editing. Our contributions are summarized as follows:

- Introducing a scene editing method through a novel neural inverse rendering for scene-scale light-field inputs in the MPI domain.
- Enhancing scene realism through global/local illumination estimation using spherical Gaussians.
- Demonstrating practical scene editing applications, highlighting our method's versatility in relighting and material appearance modifications.

2 RELATED WORK

Light fields Light fields enable various applications, including dense depth map capture (Tao et al.,), novel-view image creation (Pozo et al., 2019), depth of field refocusing (Veeraraghavan et al.,), and 3D content capturing for holographic displays (Jones et al., 2007). However, the geometry information they provide is typically sparser than that from conventional multiview setups in structure-from-motion (SfM) or neural rendering. Traditionally, light-field studies have used additional 3D scanning for accurate geometry (Wood et al., 2000; Lensch et al., 2003). Recent advances include stereo-imaging methods for dense depth maps (Hedman et al., 2017; Hedman and Kopf, 2018; Pozo et al., 2019; Kang et al., 2021) and the use of neural networks for novel view synthesis (Srinivasan et al., 2019; Flynn et al., 2019; Penner and Zhang, 2017; Choi et al., 2019). Despite these advancements, the accuracy and view angle variation remain insufficient for complete inverse rendering. Our work diverges by focusing on inverse rendering of light fields in MPI space, decomposing them into scene illumination and appearance parameters without additional geometry input.

2.1 Multi-Plane Image

Multi-plane Images (MPI) are used for novel view synthesis by mapping target image information onto multiple planes in the reference image's coordinate frame via inverse homography (Zhou et al., 2018). MPIs represent perspective geometry with parallel planes along the reference camera's view frustum, where each plane has RGB and alpha values. In an MPI with D planes, the transmittance of the d-th plane (T_d) and the rendered image color C are defined as: $T_d = \alpha_d \prod_{i=1}^{d-1}(1-\alpha_i)$. And the color of the rendering image C is: $C = \sum_{i=1}^{D}(c_d T_d)$.

Light-field image decomposition While light-field view synthesis has been widely studied (Flynn et al., 2016; Zhou et al., 2018; Srinivasan et al., 2019; Flynn et al., 2019; Penner and Zhang, 2017; Choi et al., 2019; Mildenhall et al., 2019; Broxton et al., 2020; Wang et al., 2018; Wu et al., 2017; Wizadwongsa et al., 2021), light-field image decomposition has seen less progress due to the insufficient geometry information provided by light fields alone. Recent advancements have involved making specific assumptions, like using dielectric materials for specular reflection (Tao et al., 2015; Kang et al., 2021), or formulating joint optimization problems based on view changes, albedo reflectances, and material

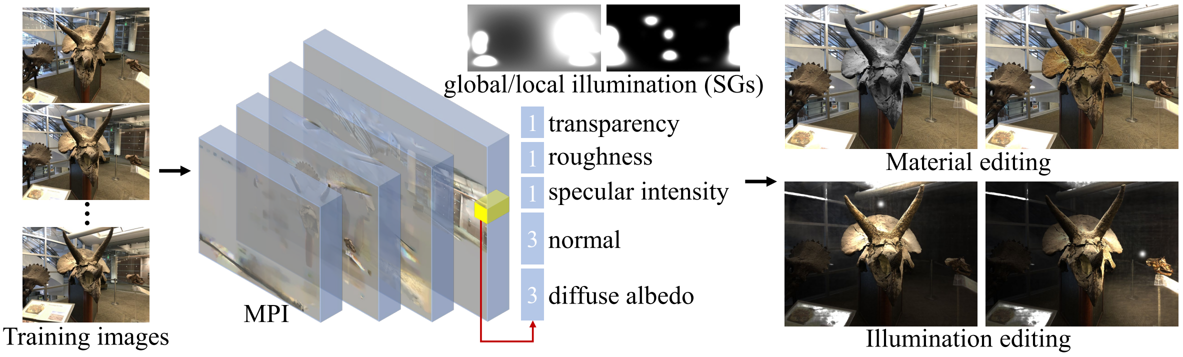

Figure 2: Our method decomposes light-field images into appearance parameters and scene illumination in multi-plane image space, enabling scene-wide manipulation of appearance and lighting.

count (Wang et al., 2016; Li et al., 2017; Ngo et al., 2019). However, these often involve unrealistic assumptions and focus mainly on depths and normals, neglecting view-dependent properties. Subsequent methods have adopted physics-based (Kang et al., 2021), classical graphics (Beigpour et al., 2018), or perception-based reflectance models (Sulc et al., 2018) for inverse rendering. Yet, these are typically formulated on the image plane (Beigpour et al., 2018) or in the 4D light-field domain (Sulc et al., 2018), limiting their suitability for efficient and interactive rendering. To address these limitations, our work proposes a decomposition method in the multi-plane image space, aiming for more efficient and interactive rendering capabilities.

Neural inverse rendering Neural inverse rendering methods such as IRON (Zhang et al., 2022a) and PS-NeRF (Yang et al., 2022) utilize images captured under varying lighting conditions for each viewpoint, with IRON focusing on edge-aware, physics-based surface rendering and PS-NeRF addressing self-occlusion in unknown lighting. These approaches yield high-quality results. Other methods, including PhySG (Zhang et al., 2021a), NerFactor (Zhang et al., 2021b), NeRV (Srinivasan et al., 2021), NeILF (Yao et al., 2022), InvRender (Zhang et al., 2022b), and TensoIR (Jin et al., 2023), operate under fixed lighting conditions. While these techniques offer various improvements, such as handling self-occlusion and indirect illumination, they do not estimate a local illumination profile. VMINER (Fei et al., 2024) models local illumination as discrete point light sources, which works well for small, distinct sources. However, for larger or more complex light sources, this method becomes computationally expensive. Our work diverges by estimating both global and local illumination as spherical Gaussians in light fields, facilitating real-time relighting and natural scene illumination adjustments and maintaining computational efficiency even with complex lighting setups. Although current state-of-the-art neural inverse rendering networks demonstrate high effectiveness in handling single objects, for example, synthetic datasets used in NeRF (Mildenhall et al., 2020), they struggle with the unique characteristics of scene-scale light-field images, such as limited numbers and specific viewpoint arrangements. Our method addresses these challenges, enabling effective use in realistic scene appearance editing and relighting.

3 LIGHT-FIELD DECOMPOSITION ON MPI

3.1 Preliminaries

Multi-plane image maps target image information onto multiple planes using inverse homography from the target to the reference image (Zhou et al., 2018). MPIs effectively visualize perspective geometry from forward-facing images. They consist of multiple parallel planes within the reference camera's view frustum, where each plane stores RGB color and alpha transparency values per pixel. In an MPI with D planes, RGB color and alpha transparency of the i-th plane are denoted as c_i and α_i, respectively, with the planes ordered from nearest to farthest from the viewpoint. The transmittance T_d of the d-th plane is given by: $T_d = \alpha_d \prod_{i=1}^{d-1}(1-\alpha_i)$. The rendered image color C is calculated as: $C = \sum_{i=1}^{D}(c_d T_d)$.

3.2 Geometry Estimation

Our approach begins with geometry estimation, followed by material and environment mapping for physics-based rendering. Given the complexity of these factors in the final rendering image, we train these parameters in stages rather than simultaneously.

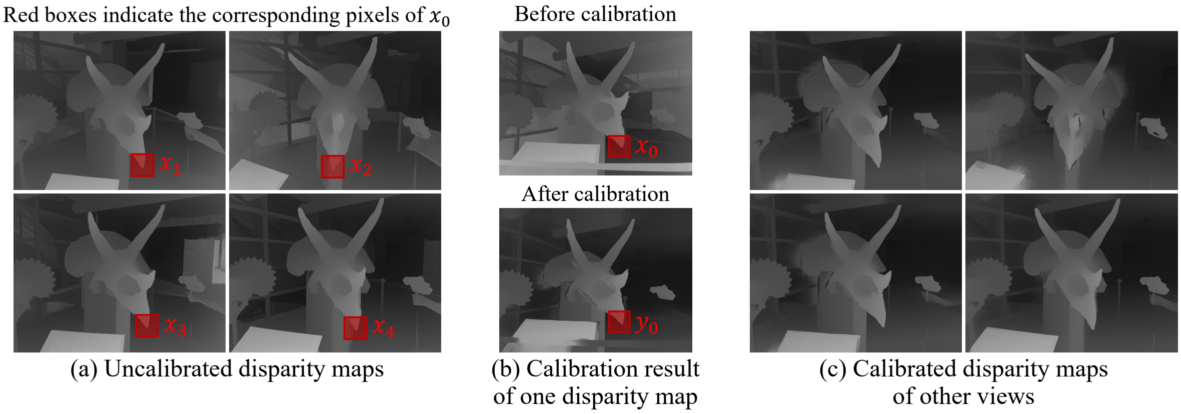

(a) Uncalibrated disparity maps

(b) Calibration result of one disparity map

(c) Calibrated disparity maps of other views

Figure 3: Multiview disparity calibration. (a) Uncalibrated disparity maps and their corresponding pixels to x_0 by optical flow. (b) Calibration result of one disparity map. (c) Calibrated disparity maps.

Initially, we establish a reference geometry, enabling MPI to train on a geometry. This involves matching pixel correspondences between the target and sub-camera images using optical flow predicted by RAFT (Teed and Deng, 2020). We then calculate the disparity map by minimizing the error in unprojecting matched samples from all camera views into world space, following Kang et al. (Kang et al., 2021). To ensure comprehensive geometry training, we compute disparity maps for all image viewpoints, not just one reference viewpoint. This is crucial as relying on a disparity map from only one viewpoint may lead to inadequate training for areas not visible from that viewpoint.

As shown in Figure 3(a), disparity maps vary with the viewpoint, leading to blurriness during training. To correct the value x_0 (the red box in Figure 3(b)), we find its corresponding pixels in other disparity maps (the red boxes in Figure 3(a)), and apply the correction using the following equation: $y_0 = \frac{1}{\beta-\alpha}\sum_{i=\alpha}^{\beta} x_i$, where α and β define the range to eliminate outliers, with $\alpha = [N \times 0.10]$ and $\beta = [N \times 0.25]$. This range was determined through experiments:

Finally, we adjust these disparity maps to align with the reference viewpoint using the extrinsic camera function.

As illustrated in Figure 4, we introduce a loss term to evaluate the difference between the alpha transparency of the MPI and the reference geometry. In an MPI with D planes, where the planes are ordered from nearest to farthest from the viewpoint, we denote the i-th plane as p_i. The alpha transparency of p_i is given, and its distance from the reference viewpoint is d_i. For a depth d obtained from the previous disparity map, we define a 1D Gaussian function $f(x)$ as: $f(x) = \exp\left(-\frac{(x-d)^2}{2\sigma^2}\right)$, where σ is the difference of disparity between planes, and the MPI's planes are equidistant in inverse depth space.

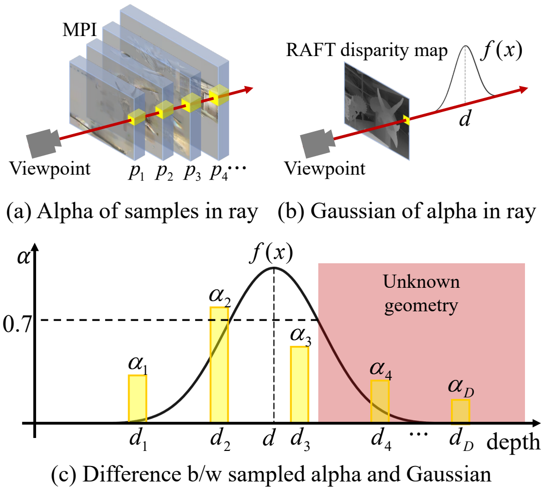

(a) Alpha of samples in ray

(b) Gaussian of alpha in ray

(c) Difference b/w sampled alpha and Gaussian

Figure 4: Geometry estimation. (a) Utilize the training viewpoint with corresponding MPI warping and sample α from the warped MPI. (b) Generate a 1D Gaussian function of depth, based on the initial disparity map from the training viewpoint. (c) Illustrate the difference between α_i and $f(x)$ along a single ray.

Considering that the disparity maps reveal depth for visible parts but not hidden geometry, our loss calculation omits differences between alpha transparency and $f(x)$ for non-visible areas. Thus, the loss between the disparity map and alpha transparency is defined as:

$$\mathcal{L}_{\text{geo}} = \frac{1}{n}\sum_{i=1}^{n}\left(\alpha_i - f(d_i)\right)^2, \qquad (1)$$

where n is the largest integer fulfilling either $(\alpha_n \leq f(d_n))$ or $(f(d_n) > 0.7)$. The geometry of the MPI was best learned when the threshold value is set to 0.7.

Disparity maps, generated for all training viewpoints, account for geometry invisible from the reference viewpoint but visible from others. The loss calculation uses the current training image viewpoint, its disparity map, and the warped MPI for that viewpoint. However, the original disparity estimation method assumes view-independent imaging, meaning surface colors do not change with viewing direction. Therefore, the initially estimated disparity map deviates from the actual disparity, limiting its use for rendering in our model like other methods using known geometry. To address this, we progressively decrease the weight of the loss by comparing alpha and disparity maps during training. This approach allows the model to initially learn approximate geometry quickly and gradually adjust to correct geometry, particularly in scenes where the initial disparity map is inaccurate due to view-dependent effects like specular highlights.

3.3 Spatially-Varying Reflectance Estimation

Our model employs physics-based rendering, differing from traditional MPI models (Mildenhall et al., 2019; Wizadwongsa et al., 2021) for view synthesis. It computes the rendering equation using geometry, material, and light environment. Traditional rendering equations involve integrating over hemispheres to account for all incident light directions. This integration, often estimated by sampling methods like Monte Carlo, is computationally expensive and undermines the primary advantage of traditional MPI, i.e., real-time rendering.

To avoid this, our approach utilizes a spherical Gaussian (SG) approximation. This assumes that the light environment comprises a mixture of SGs, and the bidirectional reflectance distribution function (BRDF) is approximated by SGs. An n-dimensional spherical Gaussian is expressed as: $G(\omega;\varepsilon,\lambda,\mu) = \mu e^{\lambda(\omega\cdot\varepsilon-1)}$, where $\omega \in \mathbb{S}^2$ represents the input, $\varepsilon \in \mathbb{S}^2$ is the lobe axis, $\lambda \in \mathbb{R}+$ denotes the lobe sharpness, and $\mu \in \mathbb{R}+^n$ is the lobe amplitude.

The significant advantage of using SG approximation in the rendering equation is the elimination of the sampling process. Since both the integral of an SG and the inner product of two SGs can be calculated in closed form, the rendering process becomes substantially more efficient and cost-effective.

In our model, we specifically employ the Cook-Torrance BRDF for our rendering process. Given the assumption that the scene comprises dielectric objects and the training images were captured with a white balance algorithm, we use a 1-dimensional Fresnel coefficient $F_0 \in \mathbb{R}+$, representing specular intensity. Additionally, we utilize 1-dimensional SGs with mono-color lobe amplitude $\mu \in \mathbb{R}+$.

The Fresnel function, based on the Schlick model and approximated by SG, is formulated as: $F(\omega_i', h) = F_0 + (1-F_0)\left(1-\cos\left(\theta_d'\right)\right)^5$, where h is a half vector between lighting direction ω_i and viewing direction ω_o, ω_i' is a vector that reflects ω_o for surface normal n, and θ_d' is the angle between ω_i' and h. Notably, when θ_d' is less than 60 degrees, the Fresnel function F closely resembles the Fresnel coefficient F_0. Therefore, we further approximate the Fresnel function as: $F(\omega_i', h) \approx F_0$.

3.4 Global and Local Illumination Estimation

Our model is designed to estimate geometry, material, and illumination for scene-scale inputs. This requires the capability to process both distant light sources, such as the sun, and nearby light sources. Traditional methods, which typically use a single environment map per scene, fall short in representing close, position-dependent light sources. To address this, we estimate two distinct types of illumination maps: a global illumination map for far-bound region and a local illumination map for near-bound region. The far-bound region refers to a region where the illumination is so far from the geometry of the MPI that it comes in at a constant direction, no matter where the incident point is located. On the other hand, the near-bound region is where the illumination is in-situ light, and its direction changes depending on the position of the incident point. Both illumination maps are formulated as a mixture of spherical Gaussian functions, allowing for a comprehensive representation of diverse lighting conditions.

Global illumination Our global illumination map, denoted as L_{far}, accounts for light sources that are infinitely distant. Such light sources provide consistent direction and intensity regardless of a point's location within the scene. We represent this map as a combination of twelve 1-D spherical Gaussians:

$$L_{\text{far}} = \sum_{k=1}^{12} G(\omega_i;\varepsilon_k,\lambda_k,\mu_k), \qquad (2)$$

where $\varepsilon_k \in \mathbb{S}^2$ represents the lobe axis, $\lambda_k \in \mathbb{R}+$ is the lobe sharpness, and $\mu_k \in \mathbb{R}_+$ indicates the lobe amplitude.

Local illumination In contrast to global illumination, local illumination in our model is represented

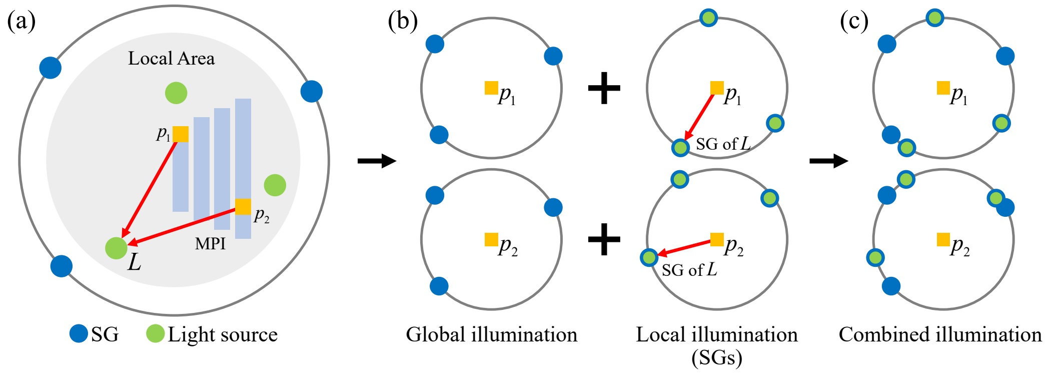

Figure 5: Global and local illumination estimation. (a) depicts virtual light sources as green circles and the spherical Gaussians of the global illumination map as blue circles. (b) shows the SGs of both global and local illumination maps for points p_1 and p_2. Note that in this figure, both blue and green circles represent SGs. (c) illustrates the combined illumination maps for points p_1 and p_2.

using virtual light sources, which vary in direction, intensity, and sharpness depending on the rendering location within the scene. Each light source is characterized by its position $x_k \in \mathbb{R}^3$, lobe sharpness $\lambda_k \in \mathbb{R}+$, and amplitude $\mu_k \in \mathbb{R}+$. These parameters determine the amplitude and sharpness when projected as spherical Gaussians in the local illumination map. The map adjusts lobe sharpness and amplitude relative to each point's distance from the light sources. Utilizing 24 virtual light sources per scene, the distance d_k from the k-th light source to a point $x \in \mathbb{R}^3$ is $d_k = \|x - x_k\|$. The local illumination map L_{near} at this point is represented as:

$$L_{\text{near}} = \sum_{k=1}^{N} G\left(\omega_i; \varepsilon'_k, \frac{\lambda_k}{d_k^2}, \frac{\mu_k}{d_k^2}\right), \tag{3}$$

where ε'_k is the normalized vector of $x - x_k$, and N is the number of virtual light sources. Thus, L_{near} comprises a mixture of N SGs. And these two local and global illuminations are integrated into one illumination map represented by SGs for each pixel, as shown in Figure 5.

Previous works like NeILF (Yao et al., 2022) and InvRender (Zhang et al., 2022b) have used point-specific environment maps, yielding high-quality results. In contrast, our method differs from InvRender in that we use virtual light sources to represent point light in the near-bound region, while InvRender uses indirect illumination. To represent the results caused by point light in the near-bound region and indirect illumination, NeILF uses illumination maps for each point of the object. However, it cannot distinguish between global illumination, indirect illumination, and point light from the learned illumination map. Our method is specially designed for appearance editing of light-field images.

This feature is beneficial for relighting tasks, such as altering the color of a specific light source or removing it entirely. Modifying lights in the light source group leads to consistent changes in the corresponding SGs within the local illumination maps. Therefore, our model incorporates both a global illumination map and a light source group, projecting the latter onto the local illumination map for each pixel in the MPI during rendering and combining it with the global illumination map for comprehensive scene illumination.

3.5 Optimization

Our model's optimization process involves several loss functions, including the geometric consistency loss $\mathcal{L}_{\text{geo}}$ from Equation (1). We employ a total variation of diffuse albedo to promote its local smoothness. The reconstruction loss is formulated as follows:

$$\mathcal{L}_{\text{rec}} = \alpha \left\| I_{\text{gt}} - I \right\|_2^2 + \beta \left\| \nabla I_{\text{gt}} - \nabla I \right\|_1, \tag{4}$$

where I represents the image synthesized by our model, and I_{gt} is the ground truth image.

The transparency loss originates from Neural volume (Lombardi et al., 2019)'s regularization term that causes the transparency value of MPI to converge to 0 or 1, defined as follows:

$$\mathcal{L}_{\text{tran}} = \sigma(1 - \sigma), \tag{5}$$

where σ is the transparency.

The total loss function, combining these elements, is defined as:

$$\mathcal{L}_{\text{total}} = \kappa\left(\mathcal{L}_{\text{rec}} + \gamma TV(\rho)\right) + \omega\left(\mathcal{L}_{\text{geo}} + 2\mathcal{L}_{\text{tran}}\right), \tag{6}$$

where ρ is the diffuse albedo, and α, β, and γ are weights balancing the loss terms, set to $\alpha = 2$, $\beta = 0.5$, and $\gamma = 0.03$. Weights ω and κ also play a role, but they are adjusted over epochs. Specifically, ω decreases and κ increases with the number of epochs, reducing the influence of $\mathcal{L}_{\text{geo}}$ and enhancing the impact of other loss terms as learning progresses. The values for ω and κ are determined as follows: $\omega = \min\left(0.5, 0.05 + 1.1^{-\frac{e-900}{50}}\right)$, and $\kappa = \min\left(1, 0.01 + 1.1^{\frac{e-801}{10}}\right)$, where e denotes the number of epochs.

4 EXPERIMENTAL RESULTS

Implementation details Our method utilizes a multilayer perceptron (MLP) for regressing pixel coordinates, a strategy chosen to minimize noise in the MPI. This MLP, taking pixel coordinates (x, y) from the d-th plane as input p, predicts alpha transparency (α) and material information for each pixel. Key to our approach is the explicit learning of spherical Gaussians (SGs) and light sources for light fields, which represent the light environment. This includes learning parameters like lobe, amplitude, and sharpness. For MPI implementation, we use 192 multiplane images, uniformly spaced in disparity space (inverse depth). The disparity range for the closest and furthest MPI from the viewpoint is determined during image calibration using SfM (SfM) (Schönberger and Frahm, 2016). In our MLP configuration, the pixel position (x, y, d) is crucial for predicting pixel-specific parameters (α, material). Positional encoding (Mildenhall et al., 2020) is applied to the pixel locations. This results in x and y being encoded into 20 dimensions and d into 16 dimensions, enhancing the model's ability to capture fine details in the MPI. Instead of using an MLP, albedo, global illumination (SGs), and local illumination (virtual light sources) are learned explicitly. A vanilla MLP with 6 layers takes 56 dimensions as input and produces 3 dimensions of output.

4.1 Quantitative Evaluation

Existing neural inverse rendering methods typically require a large number of inward-looking photographs for a target object and often struggle with a limited set of front-parallel light-field images. Among these methods, IBL-NeRF (Choi et al., 2023) stands out as it tackles scene-scale inverse rendering problems akin to our approach.

We use several light-field datasets, which are captured by large-baseline camera arrays in a structured and unstructured manner. We then use COLMAP to estimate the camera parameters. For the real image dataset, we use a real forward-facing light field dataset (Mildenhall et al., 2019), which consists of images captured by handheld smartphones. Each scene has 20 to 62 images, with a resolution of 3982×2986, which we reduce to a resolution of 1080×720 in our method. The synthetic validation rendering dataset uses the Conference and Sponza modeling files from a 3D graphics model website (McGuire, 2017) and is rendered as 512×512 resolution images from 49 viewpoints. To assess the effectiveness of our method, we conducted a comparative analysis with IBL-NeRF using this rendering dataset.

As shown in Figure 6, the estimated normals of IBL-NeRF show that the boundaries of objects in the scene are not clear and mixed, likely due to the limited number of light-field images available for input.

In contrast, our method demonstrates the capability to efficiently decompose light fields into diffuse albedo, normals, and roughness for each pixel, using an equivalent number of input images, thus achieving more accurate and detailed results. Moreover, our approach excels in learning scene geometry from light field datasets and consistently estimates uniform material properties for each object within the scene. The comparative results, as presented in Table 1, show that our method surpasses IBL-NeRF in several key aspects, including diffuse albedo, normal, roughness, and overall rendering quality.

4.2 Scene Editing Results

Our inverse rendering method was applied to a real forward-facing dataset (Mildenhall et al., 2019), consisting of scenes captured from 20 to 30 nearly identical directions. Figure 7 presents the normals, disparity, diffuse albedo, specular intensity, roughness, and both global and local illumination as estimated by our method. Despite the limited number of input sub-aperture images, our approach successfully decomposes the scene's geometry, normals, and appearance parameters. The accurate estimation of surface normals contributes to a clear separation of diffuse albedo from specular intensity, resulting in locally smooth, shading-free appearances of intrinsic albedo. The illumination profiles effectively capture the smooth/sharp and directional qualities of the scene's lighting.

Figures 8 and 9 show scene editing results, demonstrating how changes in material properties and scene illumination can be effectively implemented. Our method enables the rendering of realistic images, even when the albedo and roughness of particular objects are modified. Furthermore, by substituting the estimated global and local illuminations with a single virtual light source, we achieve renderings that accurately represent the altered illumination conditions in

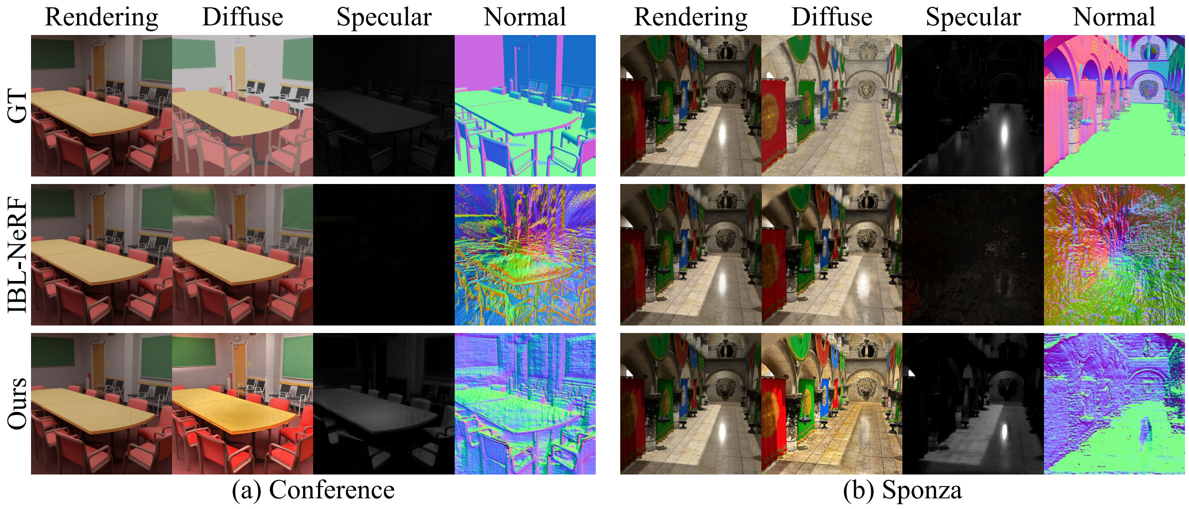

Figure 6: Compared to IBL-NeRF (Choi et al., 2023), which struggles with normal estimation due to limited input light-field images, our method effectively decomposes light fields into normal and material properties, yielding better results. Refer to Table 1 for quantitative evaluation.

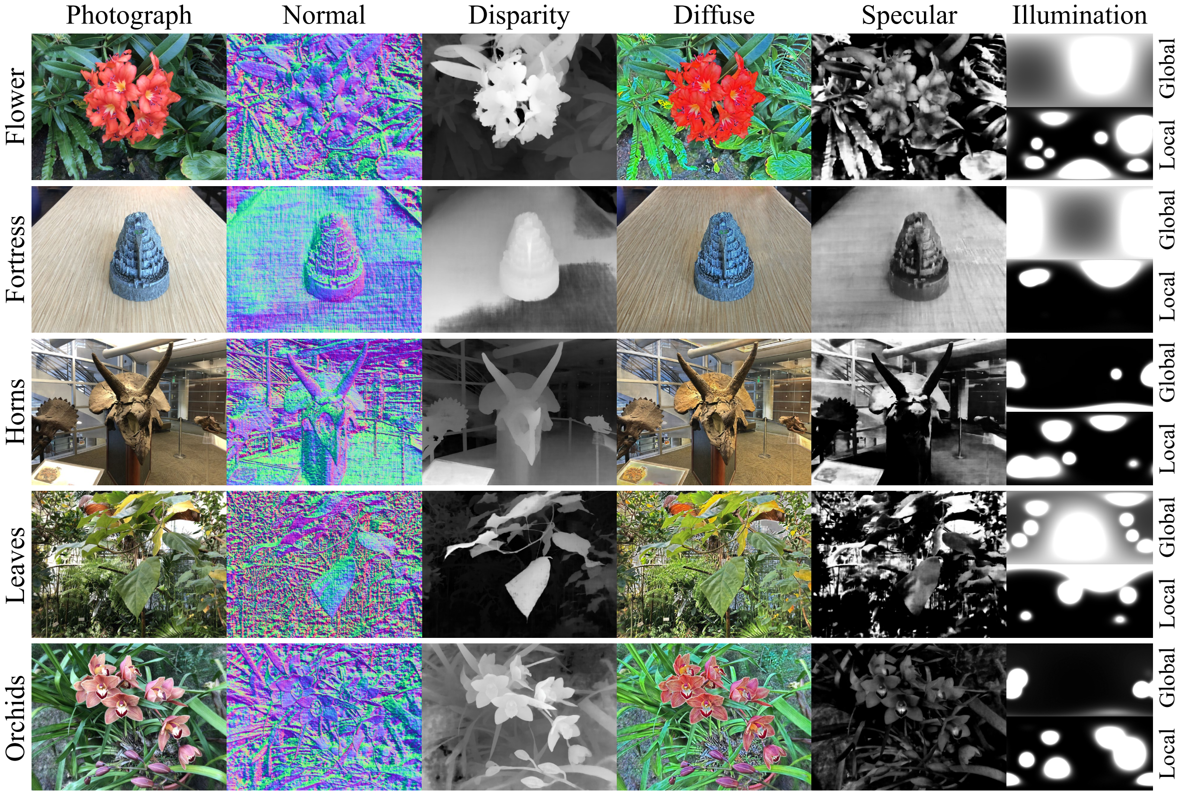

Figure 7: Decomposition results by our method with real light-field photographs (Mildenhall et al., 2019). Our method decomposes input light fields into normal, disparity, and material appearance parameters and the global/local illumination profiles of the scene as well. This allows us to edit these parameters naturally (as shown in Figure 8).

Table 1: Quantitative comparison of average scores for inverse rendering results for the rendering dataset (McGuire, 2017) obtained with IBL-NeRF (Choi et al., 2023). Green highlights indicate best accuracy.

		Conference				Sponza			
		PSNR ↑	SSIM ↑	LPIPS ↓	RMSE ↓	PSNR ↑	SSIM ↑	LPIPS ↓	RMSE ↓
Diffuse	IBL-NeRF	11.97	0.7143	0.3577	0.0635	13.44	0.6151	0.4187	0.0453
	Ours	13.87	0.6930	0.3409	0.0410	15.43	0.5645	0.3210	0.0287
Normal	IBL-NeRF	8.36	0.1599	0.9236	0.1459	8.62	0.1571	0.7835	0.1375
	Ours	12.47	0.2961	0.7576	0.0567	11.77	0.2897	0.6645	0.0665
Rendering	IBL-NeRF	38.06	0.9871	0.1771	0.00016	29.67	0.9155	0.2830	0.00109
	Ours	38.36	0.9747	0.1711	0.00015	32.81	0.9353	0.1032	0.00057

relation to the scene's surfaces. This not only validates the potential for detailed illumination editing but also underscores our method's proficiency in identifying and integrating internal light sources as part of the local illumination.

4.3 Ablation Study

Geometry Loss and Local Illumination Geometry loss and local illumination are crucial elements of our inverse rendering method. We typically use 12 SGs for global illumination and 24 virtual light sources for local illumination. To assess the impact of these components, we conduct a comparative study where we omit local illumination and instead utilize 36 SGs solely for global illumination. As shown in Figure 10, omitting geometry loss led to inaccuracies in complex scenes. Specifically, some objects that were challenging to model geometrically were rendered as translucent, erroneously revealing objects behind them. Additionally, relying solely on global illumination proved insufficient for accurately representing scene illumination, resulting in incorrect inverse rendering outcomes. These findings underscore the importance of both geometry loss and local illumination in achieving effective inverse rendering in complex scenes.

Impact of the Number of SGs The detail level in our illumination map is directly influenced by the number of spherical Gaussians: more SGs lead to a more detailed representation. However, this benefit comes at the cost of increased computational demands. To find the ideal balance between detail and efficiency, we conducted training on a real forward-facing dataset (Mildenhall et al., 2019). The global illumination does not need high-frequency patterns, so it can be represented with 12 SGs. Thus, we experimented with increasing the number of virtual light sources. Note that the number of virtual light sources influencing local illumination maps corresponds to the number of SGs in these maps. The view synthesis quality in our experiments is gauged by images syn-

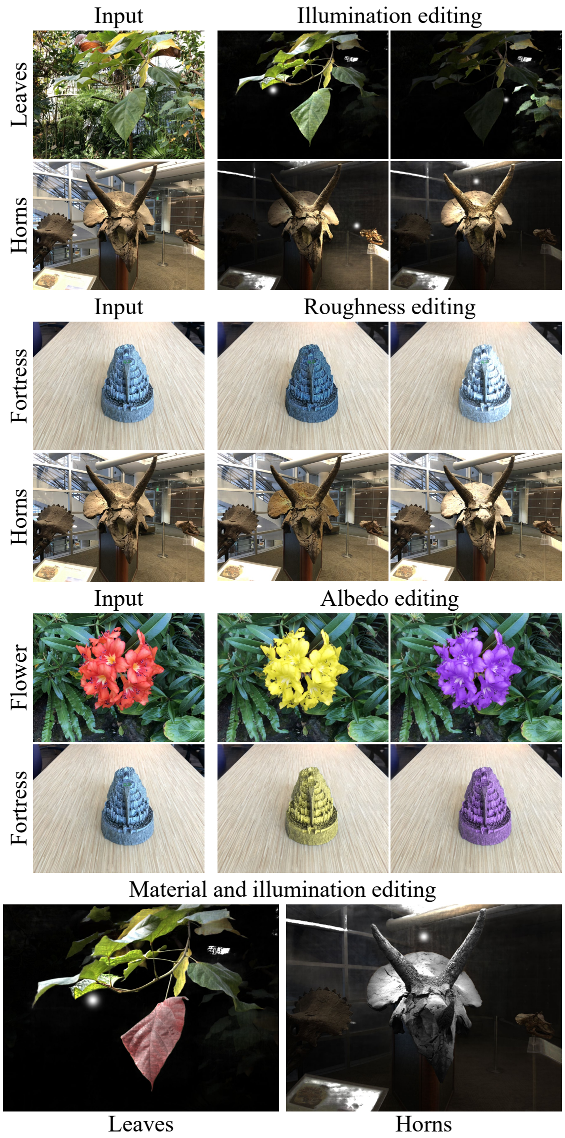

Figure 8: Our method enables real-time scene editing. This allows dynamic changes to lighting and object appearance, including color and roughness. Refer to the supplemental video for real-time relighting demonstrations.

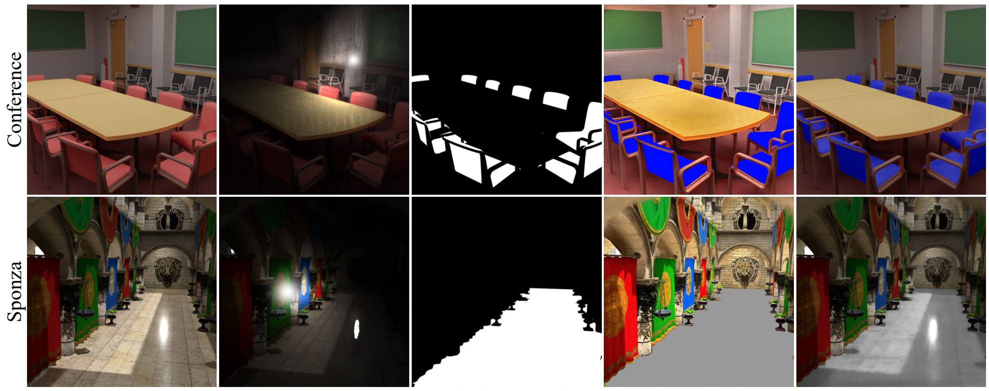

(a) Input light fields (b) Relighting result (c) Object mask (d) Edited albedo map (e) Rendering result with edited albedo

Figure 9: Additional scene editing results. (a) Input images for inverse rendering. (b) Rendered images with edited illumination. (c) Object mask of input images. (d) Albedo images with the albedo of specific objects edited. (e) Rendered images with edited albedo.

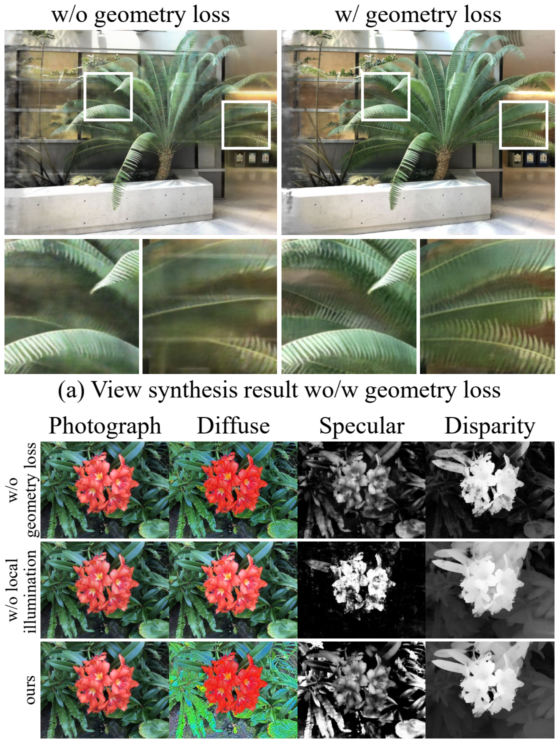

(a) View synthesis result wo/w geometry loss

(b) Inverse rendering result wo/w geometry loss and local illumination

Figure 10: Ablation study. (a) Impact of the geometry loss in terms of image quality. (b) Impact of geometry loss and local illumination estimation for inverse rendering results.

Table 2: Ablation study. Average score and rendering speed comparison according to the number of SGs for the real forward-facing dataset (Mildenhall et al., 2019). The bold numbers indicate our choice for experiments.

# of SGs (global+virtual)	PSNR↑	SSIM↑	LPIPS↓	FPS
24 (12+12)	23.92	0.848	0.270	45
36 (12+24)	**24.14**	**0.857**	**0.258**	**29**
48 (12+36)	24.19	0.856	0.254	21
60 (12+48)	24.21	0.858	0.255	16

thesized by the MLP, and the rendering time is measured from the moment MLP outputs are converted to MPI format.

Table 2 details the rendering speed performance across various counts of virtual light sources. We compare the quality and speed of view synthesis while increasing the number of virtual light sources from 12 to 48 with fixed number of SGs representing global illumination. Using real forward-facing dataset scenes at a resolution of 1080×720, our model achieves a rendering speed of 29 frames per second on an NVIDIA GeForce RTX 3090. This performance, while not matching the state-of-the-art method NeX, is notable considering the additional complexity of our model, which includes physics-based rendering and BRDF calculations. As shown in Table 2, quality scores improve as the number of virtual light sources increases, yet the improvement plateaus beyond 24 sources. Beyond this number, rendering speed decreases significantly. This trend is likely due to the relatively simple lighting conditions in the real scenes of our dataset, as opposed to more complex virtual illumination settings. Therefore, to optimize the balance between rendering quality and speed efficiency, we set the number of virtual light sources in our model to 24 and the spherical Gaussians in the global illumination map to 12.

5 DISCUSSION AND CONCLUSIONS

We have presented a neural inverse rendering method specifically designed for editing the scene-scale appearance of light-field images, incorporating elements of physics-based rendering. This approach effectively learns scene material information and lighting environments, enabling diverse scene editing tasks like relighting and altering material appearances with high fidelity. We represent geometric information as an MPI, training material data for each scene point, which is suitable for real-time neural rendering applications and ensures compatibility with traditional MPI architectures. Additionally, our method uniquely categorizes the lighting environment into far-bound and near-bound regions, adeptly handling both global and local illumination of real scenes.

As limitations, our method primarily focuses on manipulating light intensity, orientation, or hue and does not alter light relative location of point illuminations. While employing a limited number of spherical Gaussians effectively captures specular highlights, it can occasionally encounter challenges in accurately representing more complex specular phenomena, such as mirror reflections.

Also, we acknowledge the presence of checkerboard artifacts in the normal maps and black dots in the relighting results, which were noted in the supplementary video and figures. These artifacts are a consequence of the discrete structure of the MPI representation with a given spatial resolution. Setting up a higher spatial resolution for MPI representation can mitigate these issues.

ACKNOWLEDGEMENTS

Min H. Kim acknowledges the Samsung Research Funding & Incubation Center (SRFC-IT2402-02), the Korea NRF grant (RS-2024-00357548), the MSIT/IITP of Korea (RS-2022-00155620, RS-2024-00398830, 2022-0-00058, and 2017-0-00072), Microsoft Research Asia, LIG, and Samsung Electronics.

REFERENCES

Beigpour, S., Shekhar, S., Mansouryar, M., Myszkowski, K., and Seidel, H.-P. (2018). Light-Field appearance editing based on intrinsic decomposition. *Journal of Perceptual Imaging*, 1(1):010502–1–010502–1.

Broxton, M., Flynn, J., Overbeck, R., Erickson, D., Hedman, P., Duvall, M., Dourgarian, J., Busch, J., Whalen, M., and Debevec, P. (2020). Immersive light field video with a layered mesh representation. *ACM Transactions on Graphics (TOG)*, 39(4):86–1.

Choi, C., Kim, J., and Kim, Y. M. (2023). IBL-NeRF: Image-based lighting formulation of neural radiance fields. In *CGF*, volume 42, page e14929. Wiley Online Library.

Choi, I., Gallo, O., Troccoli, A., Kim, M. H., and Kautz, J. (2019). Extreme view synthesis. In *Proc. the IEEE/CVF ICCV*, pages 7781–7790.

Fei, F., Tang, J., Tan, P., and Shi, B. (2024). VMINer: Versatile multi-view inverse rendering with near-and far-field light sources. In *Proc. the IEEE/CVF CVPR*, pages 11800–11809.

Flynn, J., Broxton, M., Debevec, P., DuVall, M., Fyffe, G., Overbeck, R., Snavely, N., and Tucker, R. (2019). Deepview: View synthesis with learned gradient descent. In *Proc. the IEEE/CVF CVPR*, pages 2367–2376.

Flynn, J., Neulander, I., Philbin, J., and Snavely, N. (2016). Deepstereo: Learning to predict new views from the world's imagery. In *Proc. the IEEE/CVF CVPR*, pages 5515–5524.

Gortler, S. J., Grzeszczuk, R., Szeliski, R., and Cohen, M. F. (1996). The Lumigraph. In *Proc. the 23rd annual conference on Computer graphics and interactive techniques*, pages 43–54.

Hedman, P., Alsisan, S., Szeliski, R., and Kopf, J. (2017). Casual 3d photography. *ACM Transactions on Graphics (TOG)*, 36(6):1–15.

Hedman, P. and Kopf, J. (2018). Instant 3d photography. *ACM Transactions on Graphics (TOG)*, 37(4):1–12.

Holynski, A. and Kopf, J. (2018). Fast depth densification for occlusion-aware augmented reality. *ACM Transactions on Graphics (ToG)*, 37(6):1–11.

Jarabo, A., Masia, B., Bousseau, A., Pellacini, F., and Gutierrez, D. (2014). How do people edit light fields? *ACM Transactions on Graphics (SIGGRAPH)*, 33(4).

Jin, H., Liu, I., Xu, P., Zhang, X., Han, S., Bi, S., Zhou, X., Xu, Z., and Su, H. (2023). TensoIR: Tensorial inverse rendering. In *Proc. the IEEE/CVF CVPR*.

Jones, A., McDowall, I., Yamada, H., Bolas, M., and Debevec, P. (2007). Rendering for an interactive 360 light field display. In *ACM SIGGRAPH 2007 papers*, pages 40–es.

Kang, D., Jeon, D. S., Kim, H., Jang, H., and Kim, M. H. (2021). View-dependent scene appearance synthesis using inverse rendering from light fields. In *Proc. the IEEE ICCP*, pages 1–12. IEEE.

Lensch, H. P., Kautz, J., Goesele, M., Heidrich, W., and Seidel, H.-P. (2003). Image-based reconstruction of spatial appearance and geometric detail. *ACM Transactions on Graphics (TOG)*, 22(2):234–257.

Li, Z., Xu, Z., Ramamoorthi, R., and Chandraker, M. (2017). Robust energy minimization for brdf-invariant shape from light fields. In *Proc. the IEEE/CVF CVPR*, pages 5571–5579.

Lombardi, S., Simon, T., Saragih, J., Schwartz, G., Lehrmann, A., and Sheikh, Y. (2019). Neural volumes: Learning dynamic renderable volumes from images. *ACM Transactions on Graphics (TOG)*, 38(4):65:1–65:14.

McGuire, M. (2017). Computer graphics archive. `https://casual-effects.com/data`.

Mihara, H., Funatomi, T., Tanaka, K., Kubo, H., Mukaigawa, Y., and Nagahara, H. (2016). 4d light field segmentation with spatial and angular consistencies. In *Proc. the ICCP*.

Mildenhall, B., Srinivasan, P. P., Ortiz-Cayon, R., Kalantari, N. K., Ramamoorthi, R., Ng, R., and Kar, A. (2019). Local light field fusion: Practical view synthesis with prescriptive sampling guidelines. *ACM Transactions on Graphics (TOG)*, 38(4):1–14.

Mildenhall, B., Srinivasan, P. P., Tancik, M., Barron, J. T., Ramamoorthi, R., and Ng, R. (2020). NeRF: Representing scenes as neural radiance fields for view synthesis. In *Proc. the ECCV*.

Ngo, T.-T., Nagahara, H., Nishino, K., Taniguchi, R.-i., and Yagi, Y. (2019). Reflectance and shape estimation with a light field camera under natural illumination. *IJCV*, 127(11-12):1707–1722.

Penner, E. and Zhang, L. (2017). Soft 3D reconstruction for view synthesis. *ACM Transactions on Graphics (TOG)*, 36(6):1–11.

Pozo, A. P., Toksvig, M., Schrager, T. F., Hsu, J., Mathur, U., Sorkine-Hornung, A., Szeliski, R., and Cabral, B. (2019). An integrated 6DoF video camera and system design. *ACM Transactions on Graphics (TOG)*, 38(6):1–16.

Riegler, G. and Koltun, V. (2020). Free view synthesis. In *Proc. the ECCV*, pages 623–640. Springer.

Riegler, G. and Koltun, V. (2021). Stable view synthesis. In *Proc. the IEEE/CVF CVPR*, pages 12216–12225.

Schönberger, J. L. and Frahm, J.-M. (2016). Structure-from-motion revisited. In *Proc. the IEEE/CVF CVPR*.

Srinivasan, P. P., Deng, B., Zhang, X., Tancik, M., Mildenhall, B., and Barron, J. T. (2021). NeRV: Neural reflectance and visibility fields for relighting and view synthesis. In *Proc. the IEEE/CVF CVPR*, pages 7495–7504.

Srinivasan, P. P., Tucker, R., Barron, J. T., Ramamoorthi, R., Ng, R., and Snavely, N. (2019). Pushing the boundaries of view extrapolation with multiplane images. In *Proc. the IEEE/CVF CVPR*, pages 175–184.

Sulc, A., Johannsen, O., and Goldluecke, B. (2018). Inverse lightfield rendering for shape, reflection and natural illumination. In *Energy Minimization Methods in CVPR: 11th International Conference, EMMCVPR 2017, Venice, Italy, October 30–November 1, 2017, Revised Selected Papers 11*, pages 372–388. Springer.

Tao, M. W., Hadap, S., Malik, J., and Ramamoorthi, R. Depth from combining defocus and correspondence using light-field cameras. In *Proc. the IEEE/CVF CVPR*.

Tao, M. W., Su, J.-C., Wang, T.-C., Malik, J., and Ramamoorthi, R. (2015). Depth estimation and specular removal for glossy surfaces using point and line consistency with light-field cameras. *IEEE transactions on pattern analysis and machine intelligence*, 38(6):1155–1169.

Teed, Z. and Deng, J. (2020). RAFT: Recurrent all-pairs field transforms for optical flow. In *Proc. the ECCV*.

Veeraraghavan, A., Raskar, R., Agrawal, A., Mohan, A., and Tumblin, J. Dappled photography: Mask enhanced cameras for heterodyned light fields and coded aperture refocusing. *ACM Transactions on Graphics (TOG)*.

Wang, T.-C., Chandraker, M., Efros, A. A., and Ramamoorthi, R. (2016). SVBRDF-invariant shape and reflectance estimation from light-field cameras. In *Proc. the IEEE/CVF CVPR*, pages 5451–5459.

Wang, Y., Liu, F., Wang, Z., Hou, G., Sun, Z., and Tan, T. (2018). End-to-end view synthesis for light field imaging with pseudo 4DCNN. In *Proc. the ECCV*, pages 333–348.

Wizadwongsa, S., Phongthawee, P., Yenphraphai, J., and Suwajanakorn, S. (2021). NeX: Real-time view synthesis with neural basis expansion. In *Proc. the IEEE/CVF CVPR*, pages 8534–8543.

Wood, D. N., Azuma, D. I., Aldinger, K., Curless, B., Duchamp, T., Salesin, D. H., and Stuetzle, W. (2000). Surface light fields for 3D photography. In *SIGGRAPH*, pages 287–296.

Wu, G., Zhao, M., Wang, L., Dai, Q., Chai, T., and Liu, Y. (2017). Light field reconstruction using deep convolutional network on EPI. In *Proc. the IEEE/CVF CVPR*, pages 6319–6327.

Yang, W., Chen, G., Chen, C., Chen, Z., and Wong, K.-Y. K. (2022). PS-NeRF: Neural inverse rendering for multi-view photometric stereo. In *Proc. the ECCV*.

Yao, Y., Zhang, J., Liu, J., Qu, Y., Fang, T., McKinnon, D., Tsin, Y., and Quan, L. (2022). Neilf: Neural incident light field for physically-based material estimation. In *Proc. the ECCV*, pages 700–716. Springer.

Zhang, K., Luan, F., Li, Z., and Snavely, N. (2022a). IRON: Inverse rendering by optimizing neural sdfs and materials from photometric images. In *Proc. the IEEE/CVF CVPR*, pages 5565–5574.

Zhang, K., Luan, F., Wang, Q., Bala, K., and Snavely, N. (2021a). PhySG: Inverse rendering with spherical gaussians for physics-based material editing and relighting. In *Proc. the IEEE/CVF CVPR*, pages 5453–5462.

Zhang, X., Srinivasan, P. P., Deng, B., Debevec, P., Freeman, W. T., and Barron, J. T. (2021b). NeRFactor: Neural factorization of shape and reflectance under an unknown illumination. *ACM Transactions on Graphics (TOG)*, 40(6):1–18.

Zhang, Y., Sun, J., He, X., Fu, H., Jia, R., and Zhou, X. (2022b). Modeling indirect illumination for inverse rendering. In *Proc. the IEEE/CVF CVPR*.

Zhou, T., Tucker, R., Flynn, J., Fyffe, G., and Snavely, N. (2018). Stereo magnification: Learning view synthesis using multiplane images. In *ACM Transactions on Graphics (SIGGRAPH)*.